Magnetic Resonance Imaging 59 (2019) 17–30

Contents lists available at ScienceDirect

Magnetic Resonance Imaging

journal homepage: www.elsevier.com/locate/mri

Original contribution

SWI processing using a local phase difference modulated venous enhancement filter with noise compensation

Sreekanth Madhusoodhanan[a], Chandrasekharan Kesavadas[b], Joseph Suresh Paul[a,*]

[a] Medical Image Computing and Signal Processing Laboratory, Indian Institute of Information Technology and Management-Kerala, India
[b] Imaging Science and Interventional Radiology, Sree Chitra Tirunal Institute for Medical Science and Technology, India

ARTICLE INFO

Keywords:
Filter weight function
Mean separation
Phase mask
Noise compensation

ABSTRACT

Susceptibility weighted imaging (SWI) involves post-processing of gradient echo images which are sensitive to the spatial variations in magnetic susceptibility. The aim of this study is to develop an automated filtering scheme to enhance the contrast-to-noise ratio (CNR) and blooming on SWI. Here, the high-pass filtering for SWI processing is designed by applying a weighting function to the neighboring phase differences to enhance the susceptibility-related (SuR) contrast. This is accomplished by summing the neighboring phase differences, weighted with a scaled and shifted error function of the phase difference. Besides using the filter weights of this weighted high-pass (WHP) filter to minimize the filtering artefacts using a filter scale parameter, the CNR is further increased by introduction of the neighborhood-based noise compensation weights into the filtering process. These weights are deduced from the channel phase distribution, conditioned on the channel magnitude and noise variance. Using in vivo SWI data acquired at 1.5 T (16 nos.) and 3.0 T (30 nos.), the magnitude SWI processed using the noise compensated WHP (WHPC) filter is shown to provide an average CNR improvement of 68.40% over that of a homodyne high-pass (HHP) filter. Two tailed *t*-tests performed separately for different field strengths, show significant differences ($p < 0.001$) between mean separations of phase masks generated from the WHPC and HHP filtered phase images. In conclusion, the WHPC filter, tuned by the mean separation of the phase mask, enhances the SuR contrast of magnitude SWI for evaluation of mild cognitive impairments, brain tumor and hemorrhagic stroke.

1. Introduction

Susceptibility weighted imaging (SWI) involves post-processing the phase information from Gradient Echo (GRE) acquisition to enhance the susceptibility-related (SuR) contrast between regions [1–10]. The phase information obtained from Gradient Echo (GRE) acquisitions consist mainly of a background field induced by the main magnetic field inhomogeneities, the air-tissue interfaces, and local field variation resulting from susceptibility differences between tissues. Since the bulk phase shifts across air-tissue interfaces and brain boundaries contain low spatial frequencies, a high-pass (HP) filtering is usually performed to obtain the desired SuR information [11,12]. The SuR features in the filtered phase are further enhanced in contrast by using a non-linear mapping function to obtain a phase mask [13].

In standard SWI processing, the HF components are estimated using a homodyne high-pass (HHP) filter. This is a frequency domain filter in which the filtered image is obtained by dividing the original complex image by a low-pass (LP) Fourier filtered image [14,15] at a fixed cut-off frequency. The Fourier filtering involves a fixed size Hamming window that defines the filter strength. Longer TEs and poor shimming require stronger filters, and result in greater loss of phase contrast within larger structures. Conversely, shorter TEs are accompanied by spatial frequency overlap between intrinsic phase variations and background effects. Furthermore, residual phase wraps may occur when the filter size is too small, whereas the image contrast degrades when it is too large.

Due to the fixed cut-off frequency of the HHP filter, the filtering artefacts that may not truly represent the local SuR effects cannot be easily controlled. Thus in order to control the artefacts, it is required to vary the filter strength spatially. In conventional form of linear spatial HP filters, the filter weights are independent of the spatial location. To emphasize the SuR information, the filter weights are derived from the scaled phase differences in a local neighborhood. The data-dependent weights are estimated as a non-linear function of each neighborhood-based phase difference. The shape of this weighting function is determined such that larger phase differences are more likely to represent

* Corresponding author at: Medical Image Computing and Signal Processing Laboratory, Indian Institute of Information Technology, Trivandrum, Kerala, India.
E-mail address: j.paul@iiitmk.ac.in (J.S. Paul).

https://doi.org/10.1016/j.mri.2019.02.012
Received 19 October 2018; Received in revised form 21 February 2019; Accepted 23 February 2019

the local SuR information. The large phase weighting is not restricted to venous voxels but rather to regions laden with mineral or iron depositions where the susceptibility values are higher than the background. The blooming is essentially determined by the extent of overemphasis of the phase differences resulting from application of the filter weighting function.

We refer to this form of spatial filtering as the weighted high-pass (WHP) filter. The spatial operation is made effective by introducing statistical criteria to minimize errors arising from artefacts and noise. These are addressed by introducing 1) a global filter scale parameter that enables control of artefacts by adjusting the slope of the filter weight function, and 2) weights to check the compounding effect of noise. Information about the magnitude image and the noise level are used jointly for estimating the noise compensation weights for the WHP operation.

2. Materials and methods

2.1. SWI processing using linear spatial HP filter

As an alternative to the HHP filter, SWI phase images can also be processed using a linear form of spatial HP filter in which the filter weights are independent of spatial position. Unlike the HHP filter, spatial processing requires unwrapping of the phase images. For the current work, we have used the Laplacian based fast unwrapping method [16,17], although other forms of unwrapping, such as the Goldstein [18] or PRELUDE [19] could also have been used [20]. In order to preserve the desired SuR information at the brain boundaries and air-tissue interfaces, the unwrapped phase is subjected to background suppression. For the current work, we have used the projection onto dipole field (PDF) [21] method prior to application of the spatial filter. At any given location $r \triangleq (m,n)$, the phase filtered using the spatial HP filter is given by

$$\varphi_H(r) = \varphi_H(m,n) = \varphi(m,n) - \sum_{\substack{l,q= \\ -(N_r-1)/2}}^{(N_r-1)/2} \varphi(m+l, n+q)/N_r, \tag{1}$$

where l and q denote indices for an $N_r \times N_r$ neighborhood, and φ denotes the unwrapped phase followed by background suppression. For low-resolution data, a smaller window size of 3×3 is sufficient for spatial filtering. As the voxel size decreases, the neighborhood size should be increased so as to obtain the desired structural information.

After application of the HP filter, a normalized phase mask $\mathscr{W}$ is computed under the assumption that the HP-filtered phase is polarised in either the negative or positive direction. For example, if the phase of interest is negative, a linear mask is designed as

$$\mathscr{W}(r) = \begin{cases} [\pi + \varphi_H(r)]/\pi \; for - \pi < \varphi(r) < 0 \\ 1 \text{ otherwise,} \end{cases} \tag{2}$$

where $\varphi_H(r)$ is the HP-filtered phase at location r. The phase mask can be applied any number of times to the original magnitude image $M(r)$ to create a new image $M''(r)$, with a different contrast. The contrast enhanced image is given by

$$M''(r) = \mathscr{W}^{\Gamma}(r)\mathrm{M}(r) \tag{3}$$

Although Γ increases the contrast, the compounding effect of noise also increases, thus limiting the extent to which Γ can be increased. Therefore, similar to that of the HHP filter, increasing the number of phase mask multiplications can only improve the CNR up to a limit. With spatial filtering, further increase in CNR can be achieved by using spatially dependent weights as in the proposed WHP filter. For venous structures, this is related to the increase in the vain-based CNR (*VB-CNR*) which essentially measures the difference in intensity between the venous region and its periphery.

2.2. Weighted high-pass filtering

In order to introduce a spatially varying filtering effect, we synthesize a set of non-linear weights such that 1) the weight is an increasing function of the phase difference and 2) the weights change more rapidly with smaller phase differences and more or less saturates to unity as the phase differences become large. This is achieved by using a non-linear function such as the error function, whose magnitude is near to unity for large phase differences. Further, the filter weight function is made selective with respect to the spin direction (left or right handed) by forcing the weights to be zero for positive phase differences in a right handed system and negative phase differences in a left handed system. The resulting weighted phase differences will then be highly polarised such that the filtered phase assume more negative values in iron rich regions relative to the periphery for a right handed system such as the GE Discovery 3.0 T system.

With $i \in \{1,2,\cdots,8\}$ representing the eight neighbors of the center voxel in a 3×3 neighborhood system, the phase difference between the i'th neighbor and the central voxel is denoted by $\Delta\varphi_i$. These phase differences are used to estimate the weights for HP filtering. The filter weight functions are defined separately for both left-handed and right-handed systems [22]. The respective filter weight functions are estimated using

$$\mathrm{W}_{Fi} = 0.5\left(1 + erf\left(\frac{(\Delta\varphi_i - 2t)}{t}\right)\right), \tag{4a}$$

and

$$\mathrm{W}_{Fi} = 0.5\left(1 - erf\left(\frac{(\Delta\varphi_i + 2t)}{t}\right)\right), \tag{4b}$$

where *erf* denotes the error function and t is the scale parameter that determines the slope of the filter weight function.

Characteristic curves of the filter weight function for different t values are shown in Fig. 1. While larger phase differences are mapped to values close to unity, smaller phase differences are mapped to lower weights.

The slope of the weight function decreases with increase in the scale parameter. By adjusting this parameter globally, it is possible to tune the filter so as to retain maximum possible SuR information by simultaneously reducing the artefacts due to filtering. By weighting the phase differences between the central and the neighboring voxels and summing these across all neighborhood directions, the WHP filtered phase is obtained as

$$\varphi_{WHP} = \sum_i \mathrm{W}_{Fi}\Delta\varphi_i \tag{5}$$

2.3. Role of filter scale parameter

The role of the scale parameter t in the filtering process can be explained with reference to its dependence on the mean μ_w of the phase mask. As the histogram of the phase mask peaks at $\mathscr{W} = 1$, an increase in t will lead to a decrease in area of the tail region, accompanied by an increase in the area closer to the peak. By grouping the voxels with intensities less than μ_w into a class C_1 with mean μ_{C_1} and others into C_2 with mean μ_{C_2}, invariably relates the regions of the histogram such that an increase in μ_w is accompanied by decreasing the number of voxels with membership in C_1 and increasing the number of voxels with membership in C_2.

During the filter tuning process, t is swept through the range [0.01,0.4] with a fixed number of steps. At each step, the region C_1 will include a combination of voxels representing the true SuR effects and the filter induced artefacts. At the lower end of the range, C_1 includes a larger proportion of voxels with filtering artefacts in addition to the true SuR voxels. As t is increased in each step, more artefacts are

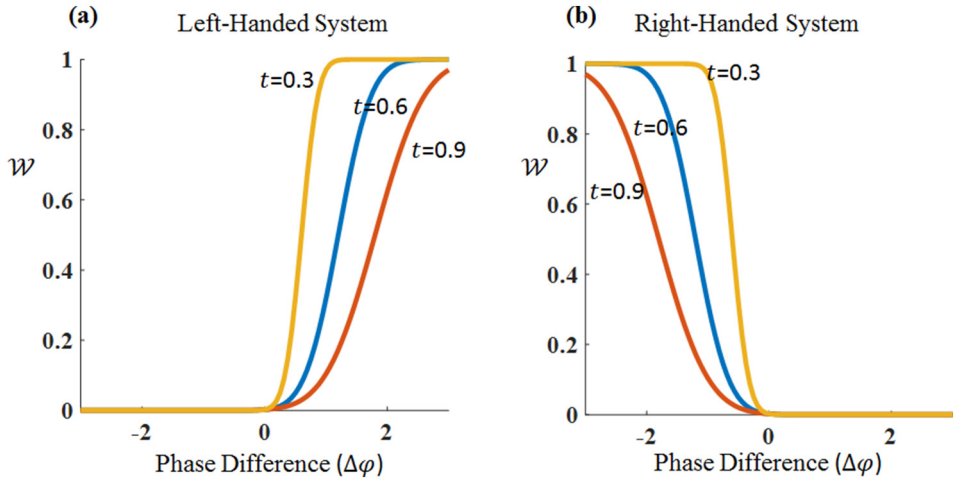

Fig. 1. WHP filter weight function shown for different scale parameter values.

removed and grouped into C_2, due to their intensities being higher than μ_w. Simultaneously, C_2 will also begin to include a small proportion of the SuR voxels that had intensities closer to and less than μ_w in the previous step. This is interpreted as a process of losing SuR information along with reduction in filtering artefacts. As more locations in the phase mask assume intensities higher than or closer to μ_w with further steps of increase in t, the number of voxels with membership in C_2 and having intensities closer to μ_w also increases. Since a desirable choice for t would be that which retains maximum voxels with true SuR effects and the least possible number of those representing artefacts, a suitable value of t would be that corresponding to the maximal mean separation $(\mu_w - \mu_{C1})$. Due to the reduced number of voxels with filter induced artefacts, this serves to choose the filter scale parameter that most reliably identifies regions laden with mineral or iron depositions such as the deep brain nuclei, or regions with hemorrhagic bleeds. Over and above this, it also serves as a statistical measure of the SuR information retained by a filtering scheme. In addition to the *VB-CNR*, we have used this measure to evaluate the WHP filtering performance in comparison to the standard HHP filter.

2.4. Noise compensation weights

To analyze the effect of noise in the filtering process, we consider a region of the phase image comprising of a vein and its periphery (background) ('p') exhibiting less negative phase in comparison to the vein center ('c'), as in a right-handed system. Corresponding intensities in the magnitude image and the signal-to-noise ratio (SNR) may still have low values at both locations. However, the influence of SNR on phase measurements at the periphery (φ_p) and the center (φ_c) will differ. This is determined by the distribution of phase, conditioned on prior information about the noise variance and the magnitude intensity at each location [23]. For a complex signal measurement with zero mean additive white Gaussian noise (AWGN) process of variance σ^2 [24], probability of the phase to assume a value in the interval $[-\pi,\pi)$, conditioned on the prior information about noise variance and magnitude intensity is given by [23]

$$P(\varphi \mid M,\sigma) = \frac{\exp(-\alpha^2)}{2\pi} \times \left\{1 + [\sqrt{\pi}\alpha\cos(\varphi - \overline{\varphi})\exp(\alpha^2\cos^2(\varphi - \overline{\varphi}))] [1 + \mathrm{erf}(\alpha\cos(\varphi - \overline{\varphi}))]\right\}, \tag{6}$$

where $\alpha = M/\sqrt{2}\sigma$, $\overline{\varphi}$ is the mean phase, and M is the magnitude intensity of the signal. Since φ_p is closer to zero within the given region, Eq. (6) reveals that for a given SNR, the influence of SNR will be higher on the edges as $P(\varphi_p|M,\ \sigma) > P(\varphi_c|M,\ \sigma)$. Thus the reliability of associating a large phase difference with an edge of a venous object in the region can only be determined by estimating $P(\varphi_p|M,\ \sigma)$ and $P(\varphi_c|M,\sigma)$ for a pair of observations (φ_c,φ_p). Generalizing this to the case where SNRs of neighboring locations are different, the influence of SNR would be higher on edges if $P(\varphi_p|M_p,\ \sigma)P(M_p) > P(\varphi_c|M_c,\ \sigma)P(M_c)$, which is equivalent to $w_p \triangleq P(\varphi_p|\sigma) > w_c \triangleq P(\varphi_c|\sigma)$. Assuming the voxel-wise measurements to be statistically independent, the influence of noise on the joint observation of a pair of neighboring phase values will be $w_c w_p$. A reliability measure for associating a pair-wise phase difference with a venous structure edge can then be deduced from the collection of such pair-wise observations across all voxels.

Since the additive noise model is only applicable to the individual channels in the context of parallel MRI (pMRI), both the above probabilistic measures have to be computed for each channel separately. Treating the noise distribution to be stationary, as in the unaccelerated case, the noise level can be assumed to be spatially independent for each channel image. However, in lieu of the differing noise variance across channels, a channel combined measure needs to be estimated for each voxel. This is obtained as

$$w = \left([w_1, w_2, \cdots w_{n_C}] \begin{bmatrix} \sigma_1^2 & \cdots & 0 \\ \vdots & \ddots & \vdots \\ 0 & \cdots & \sigma_{n_C}^2 \end{bmatrix}^{-1} [w_1, w_2, \cdots w_{n_C}]^T \right)^{\frac{1}{2}}, \tag{7}$$

where n_C is the total number of channel images. To enable usage of this channel combined measure in the spatial filtering operation involving phase differences along each neighborhood direction, we apply the notion of statistical independence to each pair of observations $(\varphi(m+l,n+q),\varphi(m,n))$ in a neighborhood centered at (m,n). Using this, a normalized reliability index for the i'th neighborhood direction at (m,n) can be defined as

$$W_{Ri}(m,n) = 1 - \frac{w(m+l,n+q)w(m,n)}{w_{max}}, \tag{8}$$

where the subscript Ri refers to the index computed for the i'th neighborhood direction involving the observations at location pair $((m+l,n+q),(m,n))$ and $w_{max} = Max\ \{w(m+l,n+q)\ w(m,n) : 1 \le m \le M, 1 \le n \le N, -(N_r-1)/2 \le (l,q) \le (N_r-1)/2\}$. Incorporation of these reliability indices for noise compensation in the filtering operation gives

$$\varphi_{WHP} = \sum_i W_{Ri} W_{Fi} \Delta\varphi_i, \tag{9}$$

where W_{Fi} denotes the corresponding filter weight derived using the error functions as in Eqs. (4a) and (4b). The implication of applying noise compensation weights (W_{Ri}) is that a phase mask derived from

Table 1
Scan parameters.

Scan parameters	1.5 T Siemens	3.0 T GE
TR	49 ms	34 ms
TE	40 ms	24.5 ms
FA	20°	15°
Slice thickness	2.2 mm	2.4 mm
Matrix	186 × 230	288 × 384
FOV	203 × 250 mm^2	168 × 240 mm^2
Bandwidth	80 Hz/pixel	325.52 Hz/pixel
Parallel imaging	GRAPPA	ARC
Average	1	1
No. of rx channels	12	12

φ_{WHP} with noise correction exhibits a less noisy appearance, but retains the same contrast for venous objects, as in a phase mask derived without noise compensation in the filtering process.

2.5. Data acquisition

All in vivo data used in this study are acquired on 3.0 T GE Discovery 750 W and 1.5 T Siemens Magnetom Avanto scanners. The scanner parameters are listed in Table 1 below.

Forty six patients, ranging in age from 24 to 76 years with a mean age of 62 years, are included in the current study. The frequency of studied patients for each neurological condition are-: 1) tumor 4(6), 2) stroke 4(8), 3) microbleed 4(6), and 4) dementia 4(10) (Numbers shown in brackets correspond to 3.0 T). This study was approved by the institution review board of our hospital, and written informed consent was obtained from all subjects.

2.6. SWI processing pipeline

The channel phase images from the GRE acquisition are first unwrapped using the Laplacian based fast unwrapping method. The noise level σ_j is estimated as the standard deviation of intensities outside the brain region in the real and imaginary components of the complex SWI signal $I_j \triangleq M_j e^{j\varphi_j}$. In a strict sense, this is to be measured at each location using a separate noise scan to account for non-stationarities due to pMRI reconstruction from the undersampled k-space data. Using this as prior information about the noise level, $P(\varphi_j \mid M_j, \sigma_j)$ is computed using Eq. (6) for each image location. To retain the conditioning on σ_j, the channel-wise weights w_j are computed by multiplying $P(\varphi_j|M_j,\sigma_j)$ by $P(M_j)$, estimated from the normalized histogram of the channel magnitude M_j. The complex multi-channel SWI data are then combined using

$$I(m,n) = \sum_{j=1}^{n_C} \frac{C_j^*(m,n)}{\sigma_j^2} I_j(m,n), \tag{10}$$

where C_j denotes the channel sensitivity map. Second, any one of the background suppression methods [21,25,26] (source codes available at https://github.com/sunhongfu/) is then applied to the channel combined phase image $\varphi \triangleq \angle I$. WHP filtering is then performed on the background-suppressed combined phase image. The proposed SWI processing pipeline is shown in Fig. 2.

3. Results

3.1. Determination of filter scale parameter

Fig. 3 illustrates the dependence of statistical measures of phase mask $\mathscr{W}$ on the filter parameter. The filter parameters are represented by the filter strength defined as the normalized Fourier domain window size for the HHP filter, and the filter scale parameter t for the WHP filter. As inferred from panels (a), both μ_{C_1} and μ_{C_2} are seen to increase with increase in the filter parameter. By varying the filter parameter over a fixed range [0.01,0.4] with hundred equal steps, the mean separations shown in panels (b) clearly indicate that the maximum mean separation of WHP filter is improved by 56% over that of HHP filter. Also, the mean separation of WHP filter exhibits a peak at the desired value of t. Panels (c) show phase masks derived from HHP (top) and WHP (bottom) filtered phase images containing deep gray nuclei in addition to veins for five different filter parameter values. For the lower end of the fixed range, the phase masks exhibit increased presence of filter induced artefacts. As the filter parameter is increased, the artefacts are reduced together with desired SuR information. For a small change in the filter parameter (10% of chosen range), it is observed that the mean separation decreases by 10% relative to the maximum value in HHP, whereas the reduction is only 3% in WHP. This indicates that the loss of SuR information, as reflected by the reduction in mean separation resulting from the step change in filter parameter, is more significant in HHP filtered SWI.

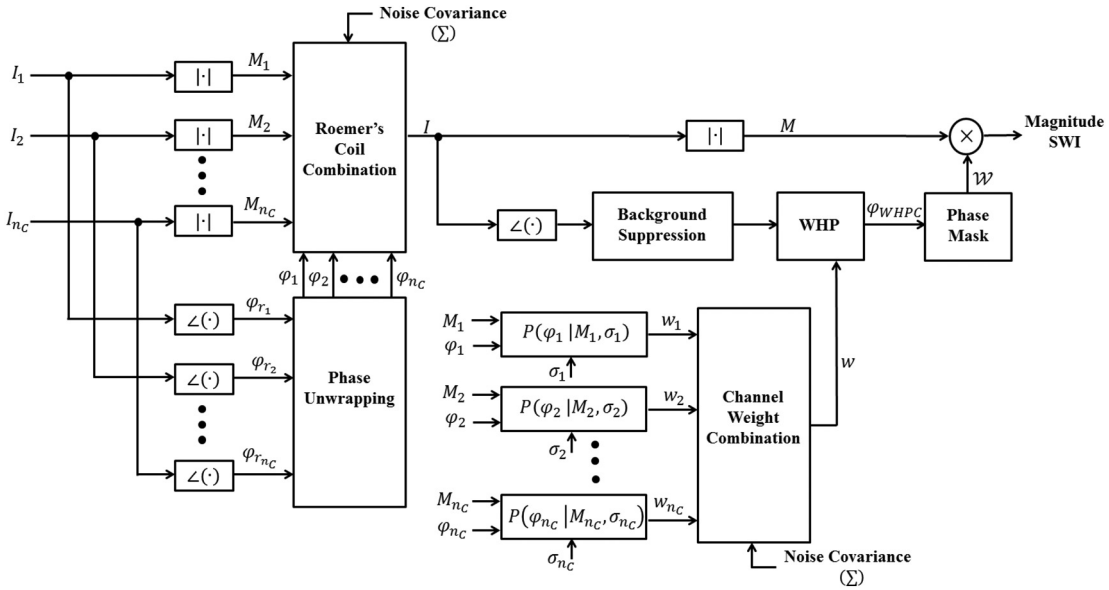

Fig. 2. Schematic block diagram of multi-channel SWI processing using the WHP filter.

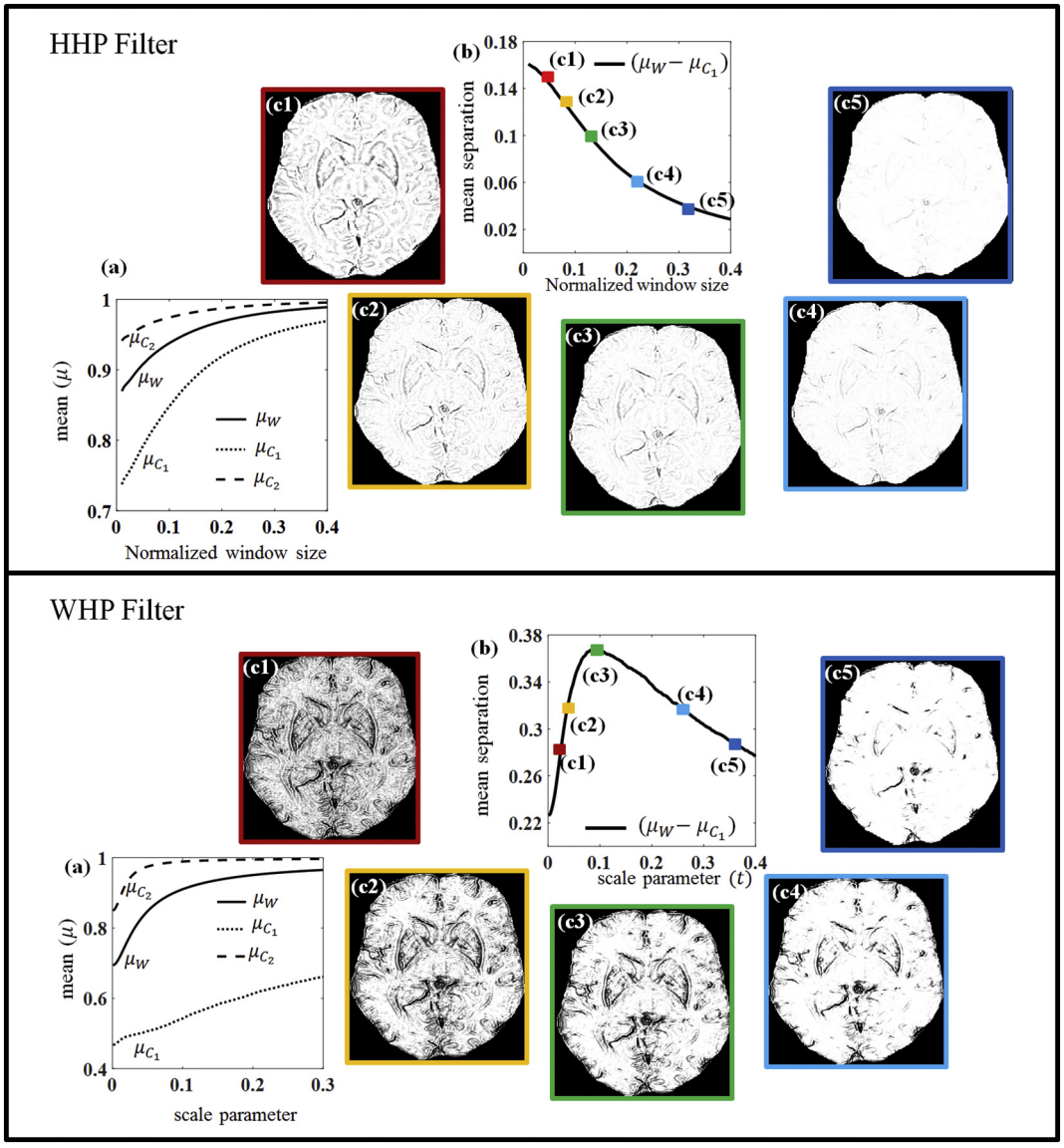

Fig. 3. Mean separation curves showing plots of mean separation as function of the filter parameter for a sample slice with deep brain nuclei. The filter parameter is the normalized Fourier domain window size for HHP filter and scale parameter t for WHP filter. (a) Plots of μ_w, μ_{C_1} and μ_{C_2} as function of filter parameter, (b) Mean separation curve, (c1-c5) Phase masks obtained using five representative filter parameter values c1-c5 as indicated on the mean separation curve.

3.2. Influence on CNR

The filtering performance is quantitatively evaluated by a vein based CNR (*VB_CNR*) defined as [27–29].

$$VB_{CNR} = \frac{S_{OUT} - S_{IN}}{\delta}, \tag{11}$$

where S_{IN} and S_{OUT} represents the mean pixel values in the venous location (red) and its surroundings, as shown in Fig. 4. δ is the standard deviation, calculated over a homogeneous region of interest not containing venous information in the channel-combined image. *VB_CNR* values for each filtering scheme measured in three different ROIs labelled R1, R2 and R3, are shown as bar graphs in Fig. 4. The in-plane profiles of voxel intensities across the venous structures in R1, R2 and R3 are plotted in the row-wise panels. The column-wise panels depict the type of filtering scheme used (HHP (Blue), WHP (Green) and WHPC (Orange)). For all ROIs, the *VB_CNR* bar graphs clearly indicate the relative CNR improvement achieved with WHP and WHPC processing.

3.3. Application to in vivo clinical studies

The sensitivity of SWI for visualization of hemorrhagic regions, microbleeds and multiple hemorrhagic foci within mass lesions provides a means for assessment of image quality improvement of SWI processed with the WHP and WHPC filters, using the respective minimum Intensity Projection (mIP) images of magnitude SWI. For mild cognitive impairments, the assessment of our filter is based on the relative increase in phase shift observed within ROIs placed in the basal ganglia region, with respect to a reference region such as the frontal white matter (FWM) or the cerebro-spinal fluid (CSF).

Figs. 5–8 show sample mIP images for tumor, stroke, microbleed and dementia, respectively. For each dataset, N_r was selected in a training phase in which the *VB-CNR* was manually estimated in a midbrain axial slice for different N_r values ranging from 3 to 11. For all clinical datasets used in this study, the maximum *VB-CNR* was obtained for $N_r = 3$. Prior to mIP generation, HP filtering was performed on the selected slices with complex data using HHP filter and unwrapped phase images using WHP and WHPC filters. To reduce the artefacts in the mIP images generated from HHP filtered images, we used the

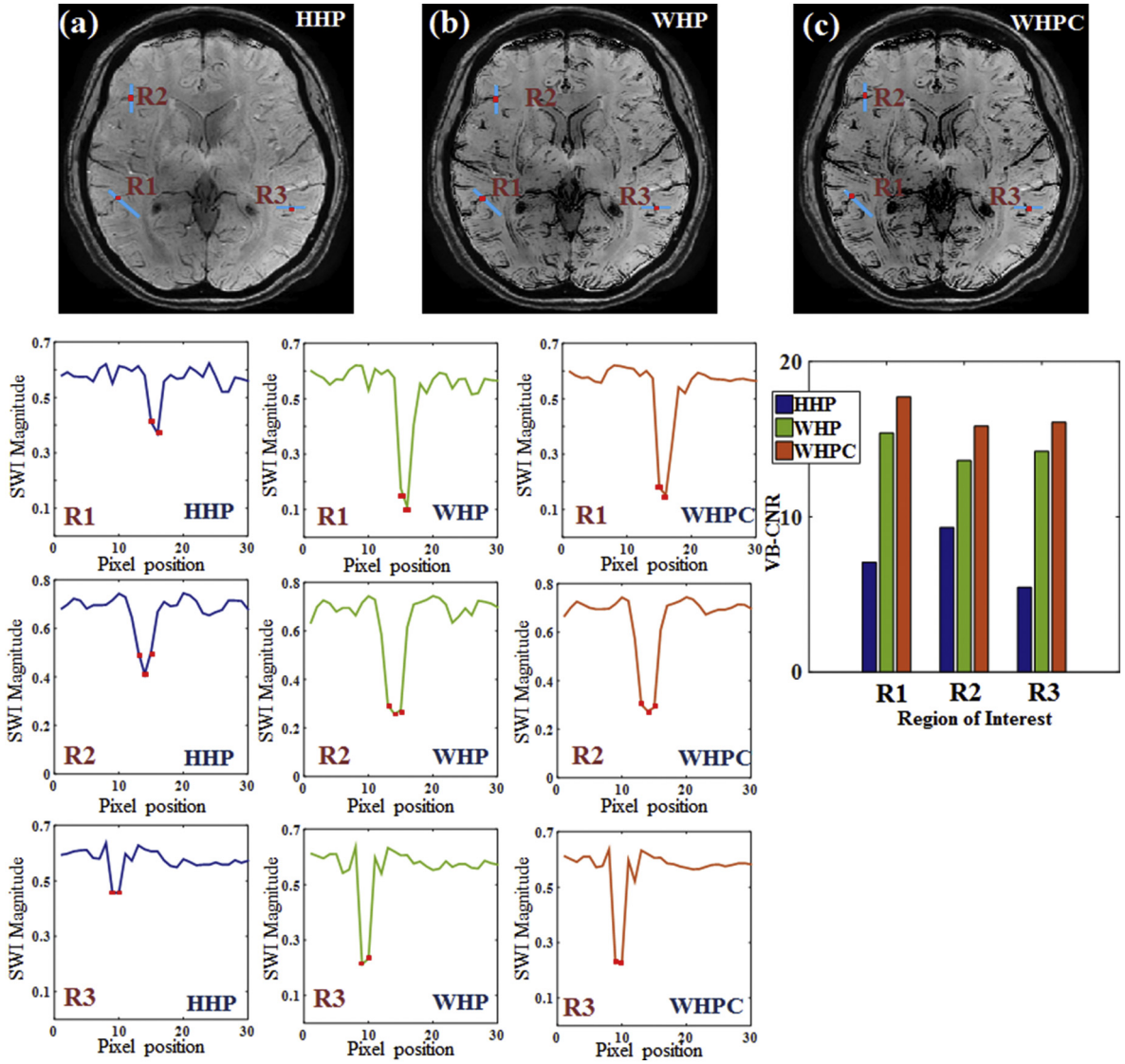

Fig. 4. Vein-based CNR (*VB_CNR*) analysis of three venous ROIs (R1, R2 and R3). Top row shows the magnitude SWI derived using (a) HHP, (b) WHP and (c) WHPC filters. Voxel intensities across the venous structures in R1, R2 and R3 are plotted in the row-wise panels. The column-wise panels show the voxel intensities for different filtering schemes used (HHP (Blue), WHP (Green) and WHPC (Orange)). In each case, the venous center is indicated by a red dot. The *VB_CNR* bar graphs clearly indicate the CNR improvement with WHP and WHPC filters for all ROIs. (For interpretation of the references to colour in this figure legend, the reader is referred to the web version of this article.)

guideline for choice of the HHP filter parameter as proposed by Haacke et al. [12]. According to this guideline, for an image with matrix size 512 × 512, a 64 × 64 central k-space data is used to obtain the low-pass filtered image which is then used to obtain the HHP filtered image by complex division. Therefore, we chose the HHP filter parameter as the normalized window size to follow the ratio 64/512. As for WHP and WHPC filters, we chose the filter scale parameter corresponding to the peak of the mean separation curve.

In each figure, the column-wise panels show mIP images for which the phase images of their constituent slices are processed using the HHP, WHP, and WHPC filters. Also, the top (a) and bottom (b) panels in each figure correspond to representative data acquired at 3.0 T and 1.5 T. For all datasets analyzed, we observe the prominence of cortical veins in the mIP images processed with WHP and WHPC filters. Whereas venous objects seen in mIPs processed with WHP and WHPC appear to have the same contrast, the mIP processed with WHP is more noisy. Furthermore, the CNRs computed across a venous object in the region highlighted using the blue line as shown in the insets, clearly indicate the superiority of the WHPC filter. The values indicate an average CNR improvement of 68.40% over the HHP filter and 18.63% over the WHP filter.

In Fig. 5(a), blooming of the peripheral structural wall due to hyper-acute bleeding in the tumor located in frontal region, is seen to be more pronounced in mIPs processed with WHP and WHPC. When compared to processing with HHP, small and faint venous structures appear more clearly with WHP and WHPC. Panels (b1)–(b3) illustrate glioma in the fronto-temporal region, with microbleeds identified near the Sylvian fissure and insular region.

In Fig. 6(a), a hemorrhagic bleed is identified in the bilateral gangliocapsular region with multi-foci microbleeds in the basal ganglia region. Among the three points of micro hemorrhagic bleed in the right putamen, two points are seen with sufficiently high blooming in the mIP processed using HHP. Also, bleeding near the right globus pallidus region appears clearly with higher blooming in WHP and WHPC processed mIPs. For bleeding in intra ventricular space as shown in panels (b), blooming in hemorrhagic transformation appears high in the WHP and WHPC processed mIPs. It is clearly observed that venous structures in the parietal and temporal regions which appear faint in the HHP

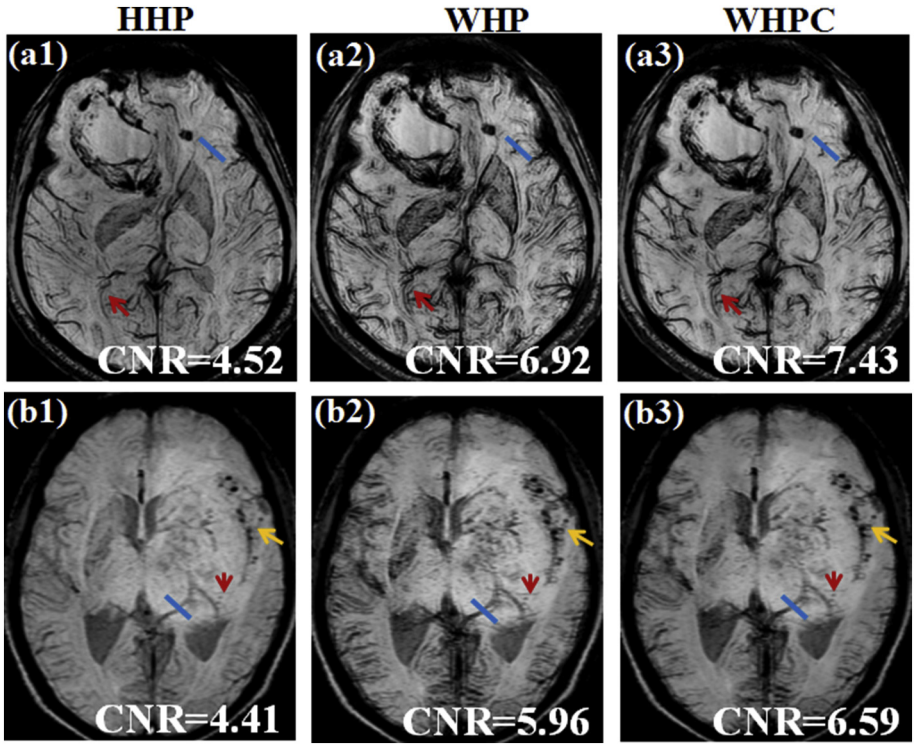

Fig. 5. Left-to-right panels show mIP SWI images obtained using (1) HHP, (2) WHP, and (3) WHPC filters of two subjects with brain tumor. Top and bottom rows show the mIP images over 8 slices of 3.0 T and 1.5 T data, with slice thickness 2.4 mm and 2.1 mm, respectively. Red arrows are used to indicate the venous structures which appear prominent with WHP and WHPC. Yellow arrows in the bottom panels highlight the improved visualization of microbleed points. (For interpretation of the references to colour in this figure legend, the reader is referred to the web version of this article.)

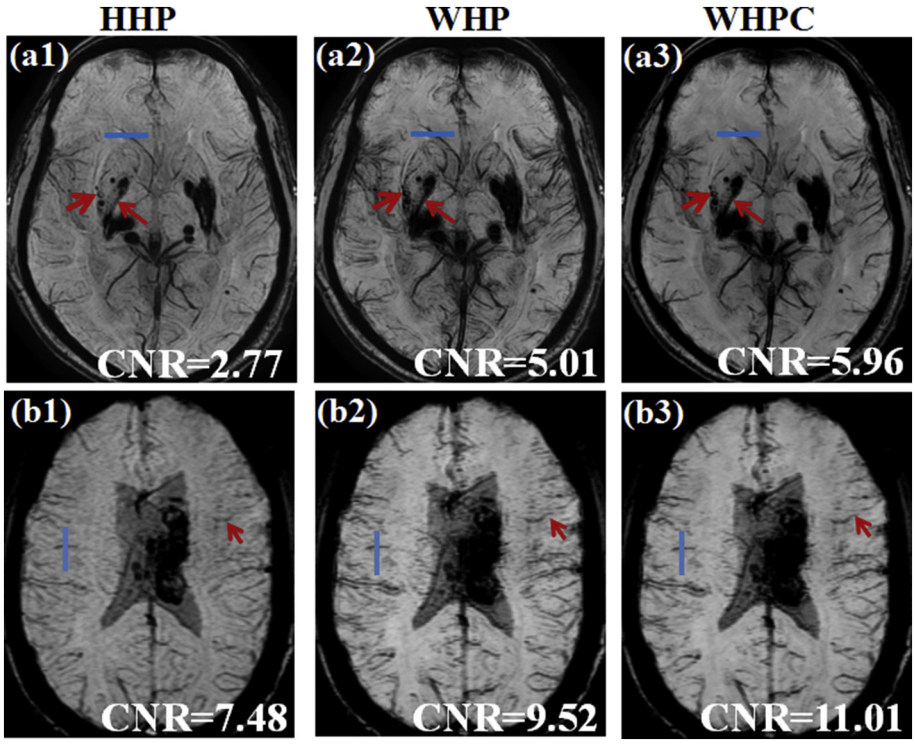

Fig. 6. Left-to-right panels show mIP SWI images obtained using (1) HHP, (2) WHP, and (3) WHPC filters of two subjects with hemorrhagic bleed. Top and bottom rows show the mIP images over 8 slices of 3.0 T and 1.5 T data with slice thickness 2.4 mm and 2.1 mm, respectively. Red arrows in the top panels highlight the microbleed foci of interest. The red arrows in the bottom panels indicate venous structures in the parietal and temporal regions. These appear faint with HHP processing, but prominently seen with processing using WHP and WHPC filters. (For interpretation of the references to colour in this figure legend, the reader is referred to the web version of this article.)

processed mIP, are more prominent in the WHP and WHPC processed mIPs.

Microhemorrhage is seen in bilateral basal ganglia and subcortical white matter in Fig. 7(a). In Fig. 7(b), the microbleed foci are seen in the frontal white matter and parietal regions, favouring the diagnosis of schwannoma. Since there is more mineral deposition in basal ganglia structures, the hypo-intense appearance of these structures in Fig. 8 shows that WHPC emphasizes the SuR contrast better than the other methods.

3.4. Statistical analysis

Paired *t*-tests are performed to evaluate differences between the mean separation values for all three filter types. The improvement in filtering performance in respect of the overall SuR information is shown by the bar graphs depicting the mean separation as a proxy measure. Top two rows in Fig. 9 shows the mean separation in tumor, stroke, microbleed and dementia data (left to right) acquired at 1.5 T (top row) and 3.0 T (second row). For each pair of filtering scheme, the symbols

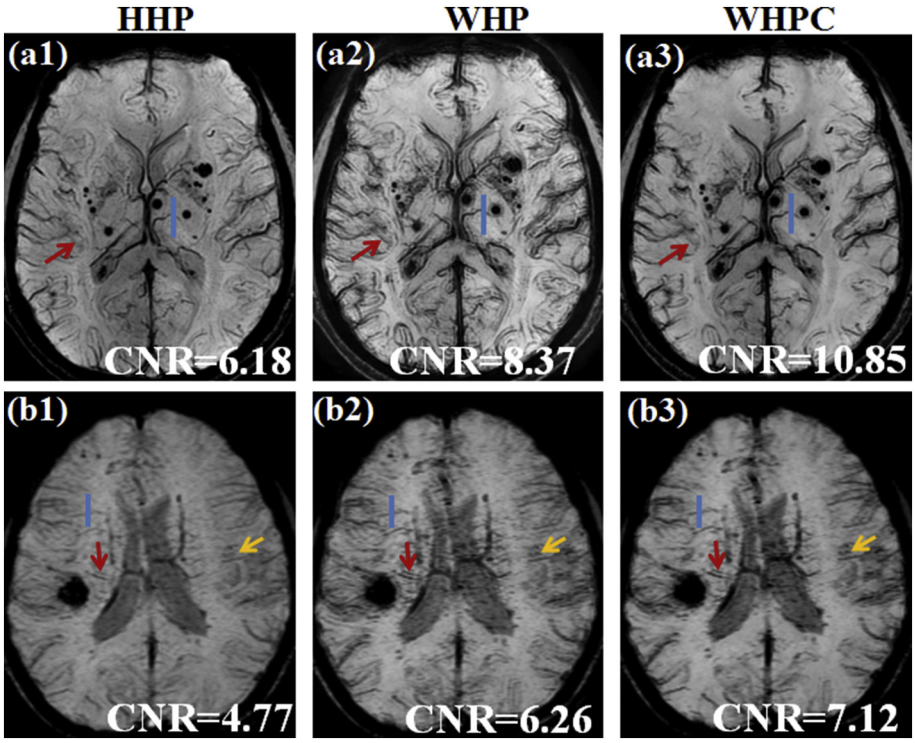

Fig. 7. Left-to-right panels show mIP SWI images obtained using (1) HHP, (2) WHP, and (3) WHPC filters of two subjects with microbleed. Top and bottom rows show the mIP images over 8 slices of 3.0 T and 1.5 T data with slice thickness 2.4 mm and 2.1 mm, respectively. Red and yellow arrows are used to indicate the faint venous structures and microbleeds which appear faint with HHP processing, but prominently seen with processing using WHP and WHPC filters. (For interpretation of the references to colour in this figure legend, the reader is referred to the web version of this article.)

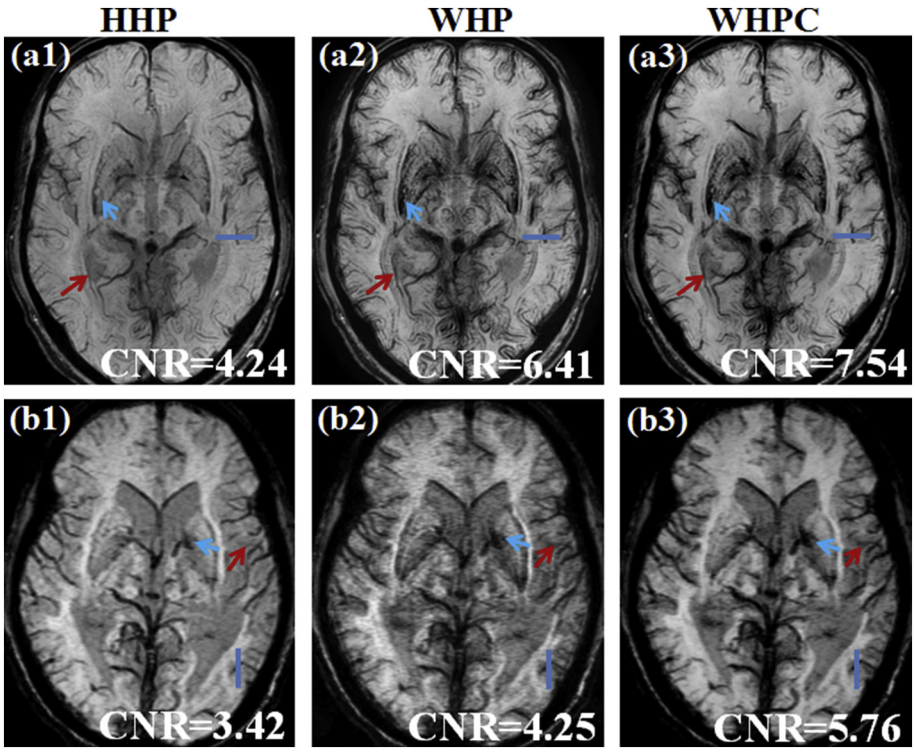

Fig. 8. Left-to-right panels show mIP SWI images obtained using (1) HHP, (2) WHP, and (3) WHPC filters of two subjects with mild cognitive impairment. Top and bottom rows show the mIP images over 8 slices of 3.0 T and 1.5 T data with slice thickness 2.4 mm and 2.1 mm, respectively. Red and blue arrow heads indicate increased prominence in the appearance of venous structures and the presence of iron deposition. (For interpretation of the references to colour in this figure legend, the reader is referred to the web version of this article.)

(*) and (#) correspond to significance levels of 0.001 and 0.05, respectively.

Motivated by prior studies using relative phase changes in frontotemporal and basal ganglia regions for quantitative assessment of cerebral iron content in subjects with mild cognitive impairment [30], phase values in the CSF and two ROIs in basal ganglia region (R_1 in the globus pallidus (GP) and R_2 in the putamen (PT)) are measured. Paired *t*-tests are then performed to evaluate the relative phase change between the CSF and the respective ROI. Panels (c1) and (c2) of Fig. 9 show bar graphs of the mean phase values (averaged across all ten dementia patients with scans taken at 3.0 T) measured in R_1 and R_2, respectively. The p-values of the paired *t*-tests for each filter type are also indicated alongside each bar graph. Among the three filter types used, the mean phase change is the highest for WHPC with a p-value $p < 0.002$.

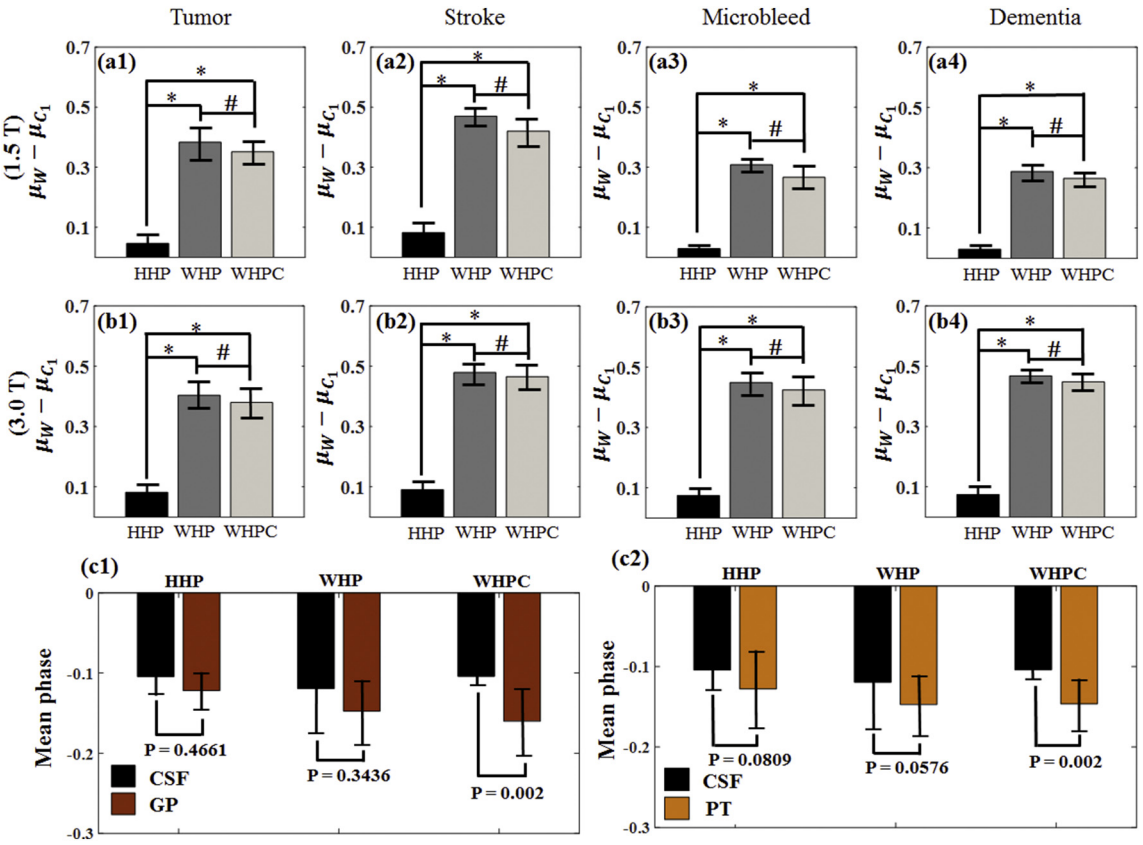

Fig. 9. Bar graphs showing mean separation in tumor, stroke, microbleed and dementia data (left to right) acquired at 1.5 T (top row) and 3.0 T (bottom row). For each pair of filtering scheme, the symbols (*) and (#) correspond to significance levels of 0.001 and 0.05, respectively. Panels (c1) and (c2) show bar graphs of the mean phase of ROIs in cerebro-spinal fluid (CSF) and the basal ganglia regions (R_1 in the globus pallidus (GP) and R_2 in the putamen (PT)). The mean phase is computed by averaging the phase values in each ROI across all ten dementia patients, with scans taken at 3.0 T. The p-values of the paired *t*-tests for each filter type are also indicated alongside each bar graph.

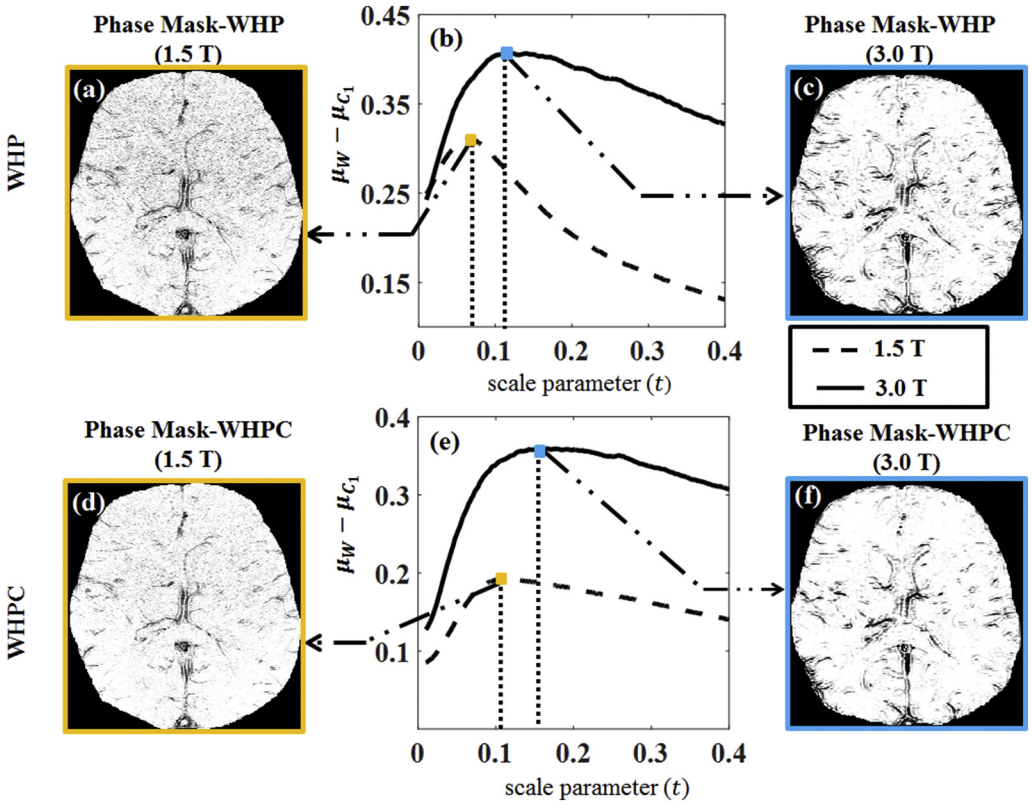

Fig. 10. Shift in scale parameter corresponding to the peak mean separation with increase in SNR. Same volunteer is scanned at both 1.5 T (dotted line) and 3.0 T (bold line). The in-plane resolutions and slice thickness are kept same in both scans. For the same filtering scheme, the SNR will higher at 3.0 T. For 3.0 T, the scale parameter corresponding to the peak mean separation is shifted to the right. Due to the effect of noise compensation, WHPC filter exhibits additional right shift in the scale parameter as compared to that of WHP filter.

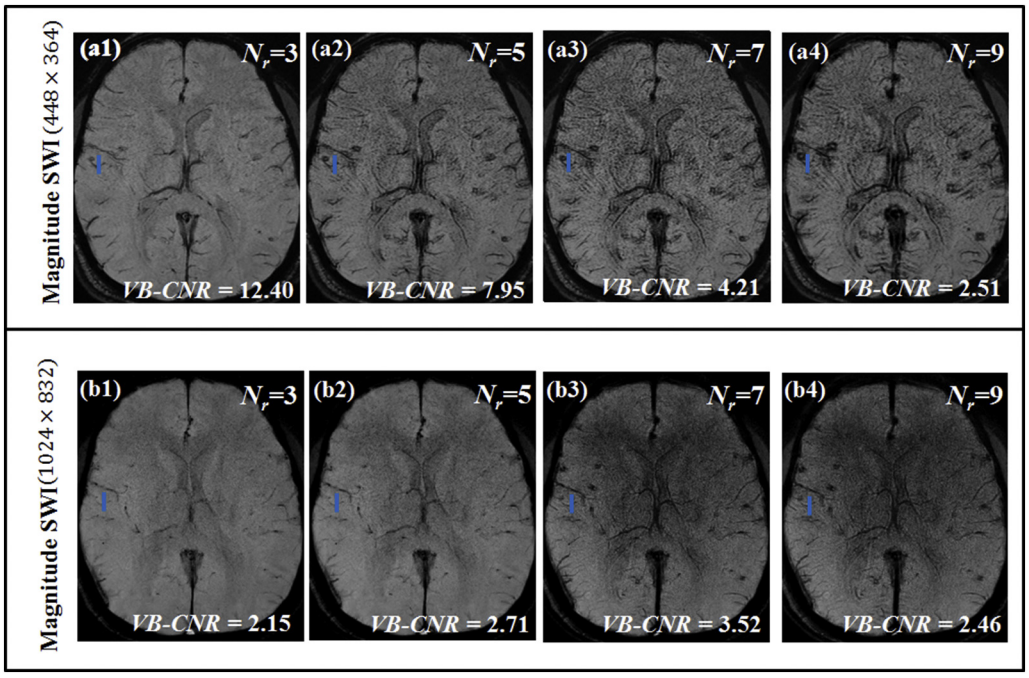

Fig. 11. Top and bottom rows show the magnitude SWI images of a volunteer scanned at 1.5 T for two different resolutions: (a) 384 × 288 and (b) 1024 × 832. Column-wise panels show the magnitude SWI images generated from phase images that are WHP filtered using different neighborhood sizes (N_r = 3, 5, 7 *and* 9). The *VB-CNR* values are shown in the insets. The blue line indicates a venous location and its surrounding pixels used for the computation of *VB-CNR*. (For interpretation of the references to colour in this figure legend, the reader is referred to the web version of this article.)

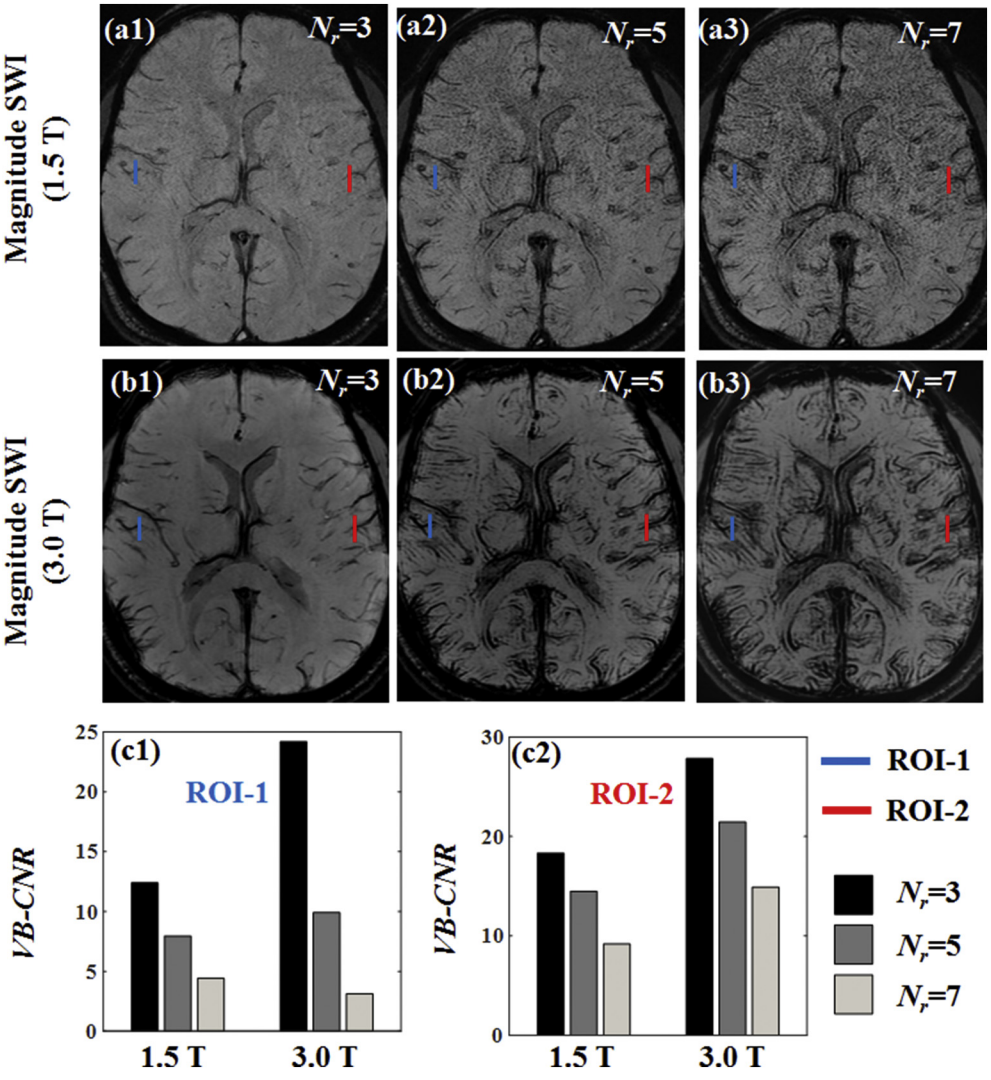

Fig. 12. Top and bottom rows show the magnitude SWI images of a volunteer scanned at two different field strengths: (a) 1. 5 T and (b) 3.0 T for same in-plane resolution of 448 × 364 and slice thickness of 2.0 mm. Column-wise panels show the magnitude SWI images generated using different neighborhood sizes (N_r). Blue and red lines indicate ROI-1 and ROI-2 depicting the venous location and its surrounding pixels used for the computation of *VB-CNR*. Bar graphs indicating *VB-CNR* computed at ROI-1 and ROI-2 are shown in panels (c1) and (c2). Irrespective of the field strength, *VB-CNR* is highest for N_r = 3 in both ROIs. (For interpretation of the references to colour in this figure legend, the reader is referred to the web version of this article.)

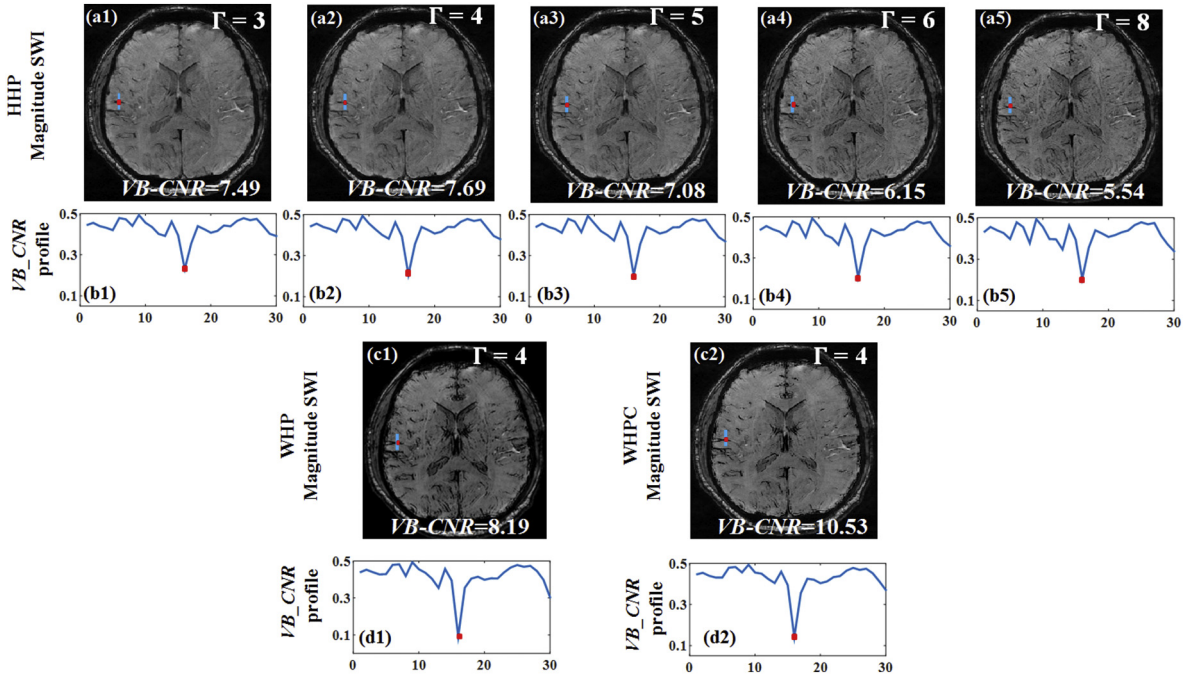

Fig. 13. CNR as function of number of phase mask multiplications. Top row shows the magnitude SWI images obtained using HHP filter for increasing number (Γ) of phase mask multiplications (left-right). Panels (b1–b4) show the *VB-CNR* profiles for increasing values of Γ across the ROI (blue line) in magnitude SWI images obtained using HHP filter. It is seen that the maximum *VB-CNR* is obtained for Γ = 4. For the purpose of comparison, panels (c1) and (c2) show the magnitude SWI images obtained using WHP and WHPC filters, respectively, with Γ = 4 number of phase mask multiplications. The corresponding *VB-CNR* profiles are shown in (d1) and (d2). It is seen that both visual quality and CNR are improved for WHP and WHPC filtered SWI as compared to that of the HHP filtered SWI. The VB-CNR is highest for WHPC filter. (For interpretation of the references to colour in this figure legend, the reader is referred to the web version of this article.)

4. Discussion

SWI sequences employing three-dimensional GRE acquisition with gradient moment nulling, exploit the differences in T2* decay resulting from intra-voxel dephasing for enhancing the sensitivity to microscopic susceptibility differences. SWI benefits from acquisition at higher field strength, as phase accumulates faster at higher field, allowing shorter TE and TR, thus less T2* decay, higher SNR, and more rapid acquisition [31,32]. All types of SWI sequences produce filtered phase images in which the paramagnetic regions exhibit oppositely signed phase values in comparison to the diamagnetic calcifications. The polarity of phase in paramagnetic regions is inherently scanner dependent, with regions of cortical veins or dural sinuses used as the reference. While scanners by Siemens and Canon use so-called “left-handed” reference schemes for which the blood products appear bright; GE and Philips use a “right-handed” reference for which these appear dark.

The SWI sequence licensed by Siemens Healthcare uses post-processing similar to that developed by Haacke et al. [12]. The SWI sequence provided by GE which is popularly known as SWAN, applies a multi-TE readout technique with post-processing reconstruction obtained as weighted averaged sum of the individual echo images. Philips offers phase difference-enhanced imaging (PADRE) with the capability for secure enhancement of an objective tissue independently of the imaging resolution. As in conventional SWI processing, PADRE uses a HHP filter to remove the low-frequency background. A phase mask is then created by application of a polynomial function of the HP filtered phase image, the highest degree of which is selected so as to maximize the CNR. With changes in image resolution, the filter size and parameters of the polynomial function are adapted so as to retain the image contrast.

To the extent that the SWI post-processing methods among different vendors are compared, the contribution in PADRE is unique due to the nature of adjustments in the phase mask parameters driven by changes in the filter size and image resolution. Similar to PADRE, the choice of the WHP filter size is also based on image resolution. However, the main distinction is that, while the phase mask parameters are empirically adapted with change in image resolution to maintain the contrast in PADRE, the SWI processing using WHP filter provides the flexibility of choosing the contrast parameter independently of the filter size. Also distinct from the HHP filter that is commonly used in SWI processing by all major vendors, the WHP filtering scheme is presented with three notable features. The first is the unique method of spatially filtering the phase to derive the desired SuR information. This uses a weighting scheme applied to the phase differences computed between each voxel and a fixed size neighborhood dependent on the image resolution. The second is the choice of a suitable filter scale parameter, fixed by adjusting the mean separation of the phase mask, for minimizing the undesirable signals. It is experimentally observed that the filter scale parameter corresponding to the maximal mean separation is also dependent on the SNR. This is shown in Fig. 10 by comparing the filter scale parameter values for a single volunteer, scanned at 1.5 T and 3.0 T, with same in-plane resolution (448 × 364) and slice thickness 2 mm. The third notable feature is the introduction of noise-compensation weights into the spatial operation in WHPC filter. As seen from the plots of mean separation for WHP and WHPC filters, further effect of SNR is observed from the shift in the peak of mean separation in WHPC to a higher value of filter scale parameter.

The dependence of WHPF performance on imaging resolution and field strength are examined further by carrying out two separate experiments. To examine the dependence on in-plane resolution, a volunteer was scanned at two different in-plane resolutions of (a) 384 × 288 and (b) 1024 × 832 for the same slice thickness (2 mm) and field strength (1.5 T). Fig. 11 shows magnitude SWI generated from the single volunteer at the two resolutions. It is observed that the *VB-CNR* is maximum at $N_r = 3$ for the low resolution data, and $N_r = 7$ for the high resolution data.

In the experiment to examine the dependence on field strength, the volunteer was scanned at two different field strengths of (a) 1.5 T and

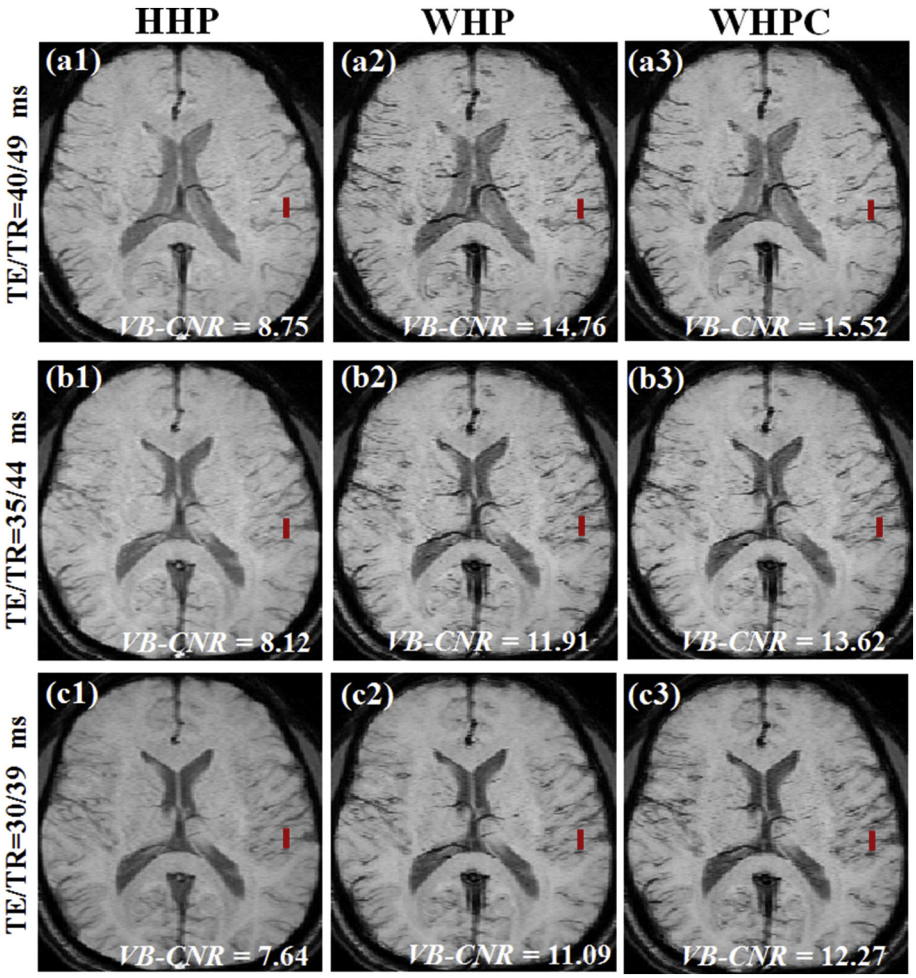

Fig. 14. Row-wise panels show the magnitude SWI images of a volunteer scanned at three different TE/TR: a) 40/49 ms, (b) 35/44 ms and (c) 30/39 ms for the same slice thickness (2.1 mm) and field strength (1.5 T). Column-wise panels show the magnitude SWI images generated using HHP, WHP and WHPC filters. Red line indicates ROI depicting the venous location and its surrounding pixels used for the computation of *VB-CNR*. The *VB-CNR* values are shown in the insets. (For interpretation of the references to colour in this figure legend, the reader is referred to the web version of this article.)

(b) 3.0 T with the same slice thickness (2 mm) and in-plane resolutions (448 × 364). Fig. 12 shows the magnitude SWI images generated from the single volunteer at 1.5 T and 3.0 T. In both the cases, the *VB-CNR* is found to be maximum at the same neighborhood size ($N_r = 3$). This shows that N_r can be fixed based on the image resolution, irrespective of the field strength. Although the processing involved is the same in both cases, the mean *VB-CNR* of 3.0 T data computed across the two ROIs (indicated by the blue and red vertical bars), is observed to be 63.50% higher compared to that of 1.5 T. The higher CNR is in accordance to the larger change in phase that is directly proportional to the field strength.

The introduction of noise compensation also enhances the CNR for given value of the contrast parameter. For a linear phase mask, the contrast is determined by the number of phase mask multiplications. For other non-linear mapping functions such as the exponential or Lorentzian function, the contrast parameter Γ appears as a scale factor of the HP filtered phase image denoted by φ_H. The exponential mask is of the form $\exp(\Gamma\varphi_{H(<0)})$, with the contrast parameter $\Gamma > 0$ in a right handed system for which $\varphi_{H(<0)} = \varphi_H$ *when* $\varphi_H < 0$ and 0 *for* $\varphi_H \geq 0$. Likewise, a Lorentzian mask with contrast parameter Γ can be generated using $1/\left(1 + \left(\frac{\varphi_H}{\Gamma}\right)^2\right)$. With any form of phase mapping function used to generate the phase mask, Γ is chosen such that the CNR of the SWI image is maximal. For HHP filtered magnitude SWI and linear phase mask, this is illustrated in Fig. 13 below. Top row shows the magnitude SWI images obtained using HHP filter for increasing values of Γ. The corresponding *VB-CNR* values are shown in the insets. It is observed that with increase in Γ, the *VB-CNR* value first increases and then decreases. This is due to the compounding effect of noise. Panels (b1)–(b4) show the *VB-CNR* profiles for increasing values of Γ. It is seen that the maximum *VB-CNR* is obtained for $\Gamma = 4$. For the purpose of comparison, panels (c1) and (c2) show the magnitude SWI images obtained using WHP and WHPC filters, respectively, with $\Gamma = 4$. The corresponding *VB-CNR* profiles are shown in (d1) and (d2). It is seen that both visual quality and CNR are improved for WHP and WHPC filtered SWI as compared to that of HHP filtered SWI. Thus in comparison to the HHP filtered SWI at $\Gamma = 4$, we observe 6.50% increase in *VB-CNR* for WHP filtered SWI and 26.97% for WHPC filtered SWI.

A main advantage of the WHP filter is the possibility of shortening the SWI measurement, due to its ability to achieve the same or better *VB-CNR* performance as that of an HHP filtered SWI acquired at a slightly longer TE/TR. The dependence of SWI contrast on TE/TR was examined by scanning a volunteer at three different TE/TRs (a) 40/49 ms, (b) 35/44 ms and (c) 30/39 ms for the same slice thickness (2.1 mm) and field strength (1.5 T). Fig. 14 shows the magnitude SWI generated using all three filtering schemes at the three TE/TRs. It is observed that both WHP and WHPC filtered magnitude SWI exhibit a higher *VB-CNR* at shorter TE/TR than the HHP filtered magnitude SWI acquired at the longer TE/TR. For example with a 12.5% reduction in TE, the venous structures are preserved with a *VB-CNR* improvement of 36% for WHP and 55% for WHPC with reference to that of HHP filter at

longer TE/TR. At the shorter TE, the HHP filter reduces the *VB-CNR* by 7%. Although shortening the TE by > 25% can lead to loss of structural information, the use of WHP and WHPC filters still exhibit *VB-CNR* improvements for venous structures that are preserved.

Apart from the aforementioned technical advantages, WHP filtering with noise compensation also provides several other benefits from a clinical perspective. In subjects with cerebrovascular bleeds, increase in blooming by the application of WHPC filter facilitates easier identification of the bleed foci. Although the blooming artefacts in SWI sequences have some intrinsic disadvantages, a useful sign would be for detecting sources of field inhomogeneities. This is because the SWI is clinically helpful for only identification and not localization of bleeds. In WHP filtering scheme, the blooming is essentially controlled by the extent of over-emphasis of the phase differences as a result of application of the filter weighting function. Apart from the effect of the filter, the blooming effect is also modulated by the acquisition parameters (field strength, slice thickness, TE, inter slice gap, TR, flip angle, and matrix size) [33,34].

The WHP filter is also found to be sensitive to changes in mild cognitive impairments, as evidenced by the relative increase in the hypo-intense gradation of the putamen structure in comparison to that revealed by HHP filter. Also in comparison to the standard SWI, the WHP processed SWI shows increased capability to differentiate the basal ganglia structures based on their SuR contrast.

Besides these major points, some of the subtle aspects of our filter can be highlighted with reference to the mIP SWI images shown in the Results section. For example, the low signal intensity bands (LSBs) in optic radiation (OR) as observed in Fig. 4(c) can be interpreted in terms of possible SuR effects induced by several potential mechanisms including iron content, myelin content or the presence of deoxyhemoglobin in the layered vascular structure adjacent to the OR [35,36]. Further, the WHPF images in Figs. 7–8 are shown to emphasize the hypointense small features involving the gray white border and sulcal veins. This may be due to the over emphasis of SuR information from local u-fibers or blood vessels in these areas as reported elsewhere [37,38]. Another possible explanation for small hypointense features is due to the diamagnetic effect of myelin proteins that may counteract the paramagnetic effect of iron, thereby contributing to the SuR contrast between gray and white matter [39–42]. It is also noticed that the transverse vein in Fig. 6(b2) (right hemisphere, red arrow) is seen to be accompanied with extra edge like structure. This type of hypointense rims involving sulcal veins have already been reported in other SWI studies [37,38].

The main limitation of our approach is the need for a training phase to determine the best possible neighborhood size for the spatial operation, especially when the acquisition is performed at a higher resolution. Additional computational cost is incurred due to the requirements of phase unwrapping, background suppression, and tuning of the filter scale parameter. Furthermore, incorporation of noise compensation in the spatial filter necessitates phase unwrapping to be performed for each channel separately, along with noise estimation. Therefore, the computational burden increases with increase in the number of channels. In pMRI with accelerated acquisition, the accuracy of noise compensation can be improved by performing a separate noise scan. It is true that the WHPF method requires the user to save and process individual channel images. However, in a more applied setting, it is possible to integrate the compensation weight calculation and provide the compensation weight map together with the DICOM images to the end user. Thus the complexity of the filtering process is limited to the need for a voxel-by-voxel calculation of the filter weights and an initial training phase in which the neighborhood size can be determined.

5. Conclusion

We have presented an HP filtering scheme for SWI, with spatially varying filter strength to emphasize the local SuR phase information. The undesirable information is rejected using a filter scale parameter tuned according to the mean separation of the phase mask. Incorporation of noise compensation weights in the filtering process using prior information about the magnitude intensity and the noise level, serves to further improve the CNR. As a post-processing method, the main advantage of this filtering scheme is that the filter parameters can be automatically tuned to provide high CNR without increasing artefacts due to filtering or noise and losing SuR information in comparison to that of HHP filter. However, it cannot be used to restore information lost due to shorter TE.

References

[1] Reichenbach JR, Venkatesan R, Schillinger DJ, Kido DK, Haacke EM. Small vessels in the human brain: MR venography with deoxyhemoglobin as an intrinsic contrast agent. Radiology. 1997;204(1):272–7.

[2] Sehgal V, Delproposto Z, Haddar D, Haacke EM, Sloan AE, Zamorano LJ, et al. Susceptibility-weighted imaging to visualize blood products and improve tumor contrast in the study of brain masses. J Magn Reson Imaging 2006;24(1):41–51.

[3] Sehgal V, Delproposto Z, Haacke EM, Tong KA, Wycliffe N, Kido DK, et al. Clinical applications of neuroimaging with susceptibility-weighted imaging. J Magn Reson Imaging 2005;22(4):439–50.

[4] Wycliffe ND, Choe J, Holshouser B, Oyoyo UE, Haacke EM, Kido DK. Reliability in detection of hemorrhage in acute stroke by a new three-dimensional gradient recalled echo susceptibilityweighted imaging technique compared to computed tomography: a retrospective study. J Magn Reson Imaging 2004;20(3):372–7.

[5] E.M. Haacke, M.I. Makki, M. Selvan, Z. Latif, J. Garbern, J. Hu, M. Law, Y. Ge. Susceptibility weighted imaging reveals unique information in multiple-sclerosis lesions using high-field MRI. In Procee of 15th annual meeting of ISMRM, Berlin. (2007). p. 2302.

[6] Raz N, Rodrigue KM, Haacke EM. Brain aging and its modifiers: insights from in vivo neuromorphometry and susceptibility weighted imaging. Ann N Y Acad Sci 2007;1097:84–93.

[7] Tong KA, Ashwal S, Obenaus A, Nickerson JP, Kido DK, Haacke EM. Susceptibility-weighted MR imaging: a review of clinical applications in children. Am J Neuroradiol 2008;29(1):9–17.

[8] Haacke EM, Cheng NY, House MJ, Liu Q, Neelavalli J, Ogg RJ, et al. Imaging iron stores in the brain using magnetic resonance imaging. Magn Reson Imaging 2005;23(1):1–25.

[9] Barth M, Nobauer-Huhmann IM, Reichenbach JR, Mlynarik V, Schoggl A, Matula C, et al. High-resolution three-dimensional contrastenhanced blood oxygenation of brain tumors at 3 tesla: first clinical experience and comparison with 1.5 Tesla. Investig Radiol 2003;38(7):409–14.

[10] Adams LC, Bressem K, Böker SM, Bender YN, Nörenberg D, Hamm B, et al. Diagnostic performance of susceptibility-weighted magnetic resonance imaging for the detection of calcifications: a systematic review and meta-analysis. Sci Rep 2017;7(1):15506.

[11] Wang Y, Yu Y, Li D, Bae KT, Brown JJ, Lin W, et al. Artery and vein separation using susceptibility-dependent phase in contrast-enhanced MRA. J Magn Reson Imaging 2000;12(5):661–70.

[12] Haacke EM, Mittal S, Wu Z, Neelavalli J, Cheng YC. Susceptibility-weighted imaging: technical aspects and clinical applications, part 1. Am J Neuroradiol 2009;30(1):19–30.

[13] Quinn MP, Gati JS, Klassen LM, Lin AW, Bird JR, Leung SE, et al. Comparison of multiecho postprocessing schemes for SWI with use of linear and nonlinear mask functions. Am J Neuroradiol 2014;35(1):38–44.

[14] Haacke EM, Xu Y, Cheng YC, Reichenbach JR. Susceptibility weighted imaging (SWI). Magn Reson Med 2004;52(3):612–8.

[15] Rauscher A, Barth M, Herrmann KH, Witoszynskyj S, Deistung A, Reichenbach JR. Improved elimination of phase effects from background field inhomogeneities for susceptibility weighted imaging at high magnetic field strengths. Magn Reson Med 2008;26(8):1145–51.

[16] Schofield MA, Zhu Y. Fast phase unwrapping algorithm for interferometric applications. Opt Lett 2003;28(14):1194–6.

[17] Li W, Avram AV, Wu B, Xiao X, Liu C. Integrated Laplacian-based phase unwrapping and background phase removal for quantitative susceptibility mapping. NMR Biomed 2014;27(2):219–27.

[18] Goldstein RM, Zebker HA, Werner CL. Satellite radar interferometry: two-dimensional phase unwrapping. Radio Sci 1988;23(4):713–20.

[19] Jenkinson M. Fast, automated, *N*-dimensional phase-unwrapping algorithm. Magn Reson Med 2003;49(1):193–7.

[20] Robinson SD, Bredies K, Khabipova D, Dymerska B, Marques JP, Schweser F. An illustrated comparison of processing methods for MR phase imaging and QSM: combining array coil signals and phase unwrapping. NMR Biomed 2017;30(4):e3601.

[21] Liu T, Khalidov I, de Rochefort L, Spincemaille P, Liu J, Tsiouris AJ, et al. A novel background field removal method for MRI using projection onto dipole fields. NMR Biomed 2011;24(9):1129–36.

[22] Mehemed TM, Yamamoto A. High-pass-filtered phase image: left-versus right-handed MR imaging systems. Am J Neuroradiol 2013;34(6):E72.

[23] Chung AC, Noble JA, Summers P. Fusing speed and phase information for vascular segmentation of phase contrast MR angiograms. Med Image Anal 2002;6(2):109–28.
[24] Aja-Fernández S, Tristán-Vega A. A review on statistical noise models for magnetic resonance imaging. LPI, ETSI Telecomunicacion, Universidad de Valladolid, Spain. Tech Rep 2013.
[25] Schweser F, Lehr BW, Andreas D, Rainer RJ. Sophisticated harmonic artifact reduction for phase data (SHARP). Med: Proceeding Proc. GC Intl. Soc. Mag. Reson; 2010.
[26] Zhou D, Liu T, Spincemaille P, Wang Y. Background field removal by solving the Laplacian boundary value problem. NMR Biomed 2014;27(3):312–9.
[27] Borrelli P, Palma G, Tedeschi E, Cocozza S, Comerci M, Alfano B, et al. Improving signal-to-noise ratio in susceptibility weighted imaging: a novel multicomponent non-local approach. PLoS One 2015;10(6):e0126835.
[28] Borrelli P. Denoising in magnetic resonance imaging: theory, algorithms and applications. PhD Thesis. Università degli Studi di Napoli Federico II; 2015.
[29] Jang U, Nam Y, Kim DH, Hwang D. Improvement of the SNR and resolution of susceptibility-weighted venography by model-based multi-echo denoising. Neuroimage. 2013;70:308–16.
[30] Sheelakumari R, Kesavadas C, Varghese T, Sreedharan RM, Thomas B, Verghese J, et al. Assessment of iron deposition in the brain in frontotemporal dementia and its correlation with behavioral traits. Am J Neuroradiol 2017;38(10):1953–8.
[31] Reichenbach JR, Barth M, Haacke EM, Klarhöfer M, Kaiser WA, Moser E. High-resolution MR venography at 3.0 Tesla. J Comput Assist Tomogr 2000;24(6):949–57.
[32] Wu B, Li W, Avram AV, Gho SM, Liu C. Fast and tissue-optimized mapping of magnetic susceptibility and T2* with multi-echo and multi-shot spirals. Neuroimage. 2012;59(1):297–305.
[33] T. Kaaouana. Detection and characterization of cerebral microbleeds: application in clinical imaging sequences on large populations of subjects ((Doctoral dissertation), University PIERRE ET MARIE CURIE, Paris).
[34] S.M. Gregoire. Cerebral microbleeds as a marker of small vessel disease: new insights from neuro-imaging and clinical studies in stroke patients ((Doctoral dissertation), UCL (University College London)).
[35] Mori N, Miki Y, Kasahara S, Maeda C, Kanagaki M, Urayama SI, et al. Susceptibility-weighted imaging at 3 Tesla delineates the optic radiation. Investig Radiol 2009;44(3):140–5.
[36] Ide S, Kakeda S, Korogi Y, Yoneda T, Nishimura J, Sato T, et al. Delineation of optic radiation and stria of Gennari on high-resolution phase difference enhanced imaging. Acad Radiol 2012;19(10):1283–9.
[37] Hodel J, Outteryck O, Verclytte S, Deramecourt V, Lacour A, Pruvo JP, et al. Brain magnetic susceptibility changes in patients with natalizumab-associated progressive multifocal leukoencephalopathy. Am J Neuroradiol 2015;36(12):2296–302.
[38] Halefoglu AM, Yousem DM. Susceptibility weighted imaging: clinical applications and future directions. World J Radiol 2018;10(4):30.
[39] Fukunaga M, Li TQ, van Gelderen P, de Zwart JA, Shmueli K, Yao B, et al. Layer-specific variation of iron content in cerebral cortex as a source of MRI contrast. Proc Natl Acad Sci U S A 2010;107:3834–9.
[40] He X, Yablonskiy DA. Biophysical mechanisms of phase contrast in gradient echo MRI. Proc Natl Acad Sci U S A 2009;106:13558–63.
[41] Zhong K, Ernst T, Buchthal S, Speck O, Anderson L, Chang L. Phase contrast imaging in neonates. Neuroimage 2011;55:1068–72.
[42] C. Langkammer, N. Krebs, W. Goessler, E. Scheurer, K. Yen, F. Fazekas, S. Ropele. Susceptibility induced gray–white matter MRI contrast in the human brain. Neuroimage. 16; 59 (2) (2012) 1413–9.